Supplementary Information B

Joseph Daafour, Bing Ni, Pascal Bassène, Chiu Tai Law, Moussa N'Gom, and Nicholas Kotov**

Dr. Bing Ni, Prof. Nicholas Kotov
Department of Chemical Engineering and Department of Materials Science and Engineering University of Michigan Ann Arbor, MI 48109, USA
E-mail: kotov@umich.edu

Prof. Chiu Tai Law
Electrical Engineering and Computer Science Department, University of Wisconsin, Milwaukee, WI 53201, USA.

Joseph Daafour[1], Dr. Pascal Bassène[1,2,3], and Prof. Moussa N'Gom[1,2]
[1] Department of Physics, Applied Physics, and Astronomy Rensselaer Polytechnic Institute (RPI), 110 8th St., Troy, NY 12180, USA.
[2] The Shirley Ann Jackson, PhD. Center for Biotechnology and Interdisciplinary Studies, RPI, 110 8th St, Troy, NY 12180, USA.
[3] Center for Materials, Devices and Integrated Systems (CMDIS), Low center, RPI, 110 8th St, Troy, NY 12180, USA.
E-mail: ngomm@rpi.edu; kotov@umich.edu;

A0.1 Simulation of the electric field under different wavelengths

The electron tomography reconstruction captures the geometry of the twisted NR, the result is further used as the input for the electromagnetic simulations of the gold NRs (Figure shown below).

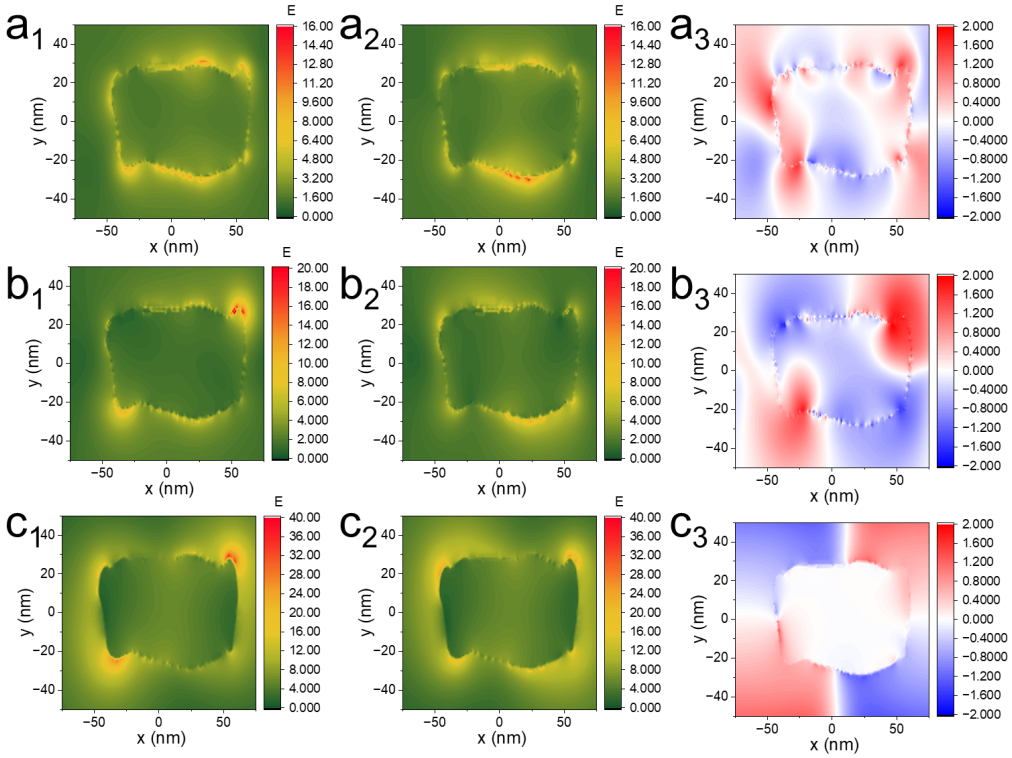

Fig. S1. Electric field mapping under different wavelengths. (a) 541 nm; (b) 619 nm; (c) 803 nm. The first two columns indicate the incident light polarization, σ^- and σ^+, respectively. The last column marks the electric field difference by calculating the results of $2(|E_{\sigma^-}|^2 - |E_{\sigma^+}|^2)/(|E_{\sigma^+}|^2 + |E_{\sigma^-}|^2)$.

Although the peak positions in the simulated extinction spectrum were slightly blue-shifted compared to the experimental result, the shape of the simulation resembles the experimental result. This might be due to the limited variations of the particle shapes in the simulation. Particle dispersion solutions were used in the experimental measurements; therefore, obtained results were the average of all particles.

However, the wet-chemical synthesis could not lead to perfect size uniformity, i.e., the NR shapes and sizes must vary in some range, and these variations would lead to slightly different optical properties. If more 3D structures of particles can be captured and used in the electromagnetic simulations, the results should be closer to the experimental results. The same applies to the g-factor plot simulations. The simulated g-factor plot assumed a shape and intensity similar to those of the experimental results, with peaks slightly blue-shifted. Overall, these simulation results suggested that the simulation captures the fundamental features of the twisted NRs.

In Fig. S1, the electric field distributions around the NRs are shown below. Three wavelengths based on the simulated peaks in the extinction spectrum and g–factor plots (541 nm, 619 nm, and 803 nm) were selected to induce the near-field effect. At 541 nm Fig. S1(a),

the most intense electric field is populated at the lateral positions of the rod (σ^-: upper side, σ^+, lower side). At longer wavelengths in Fig. S1(b, c), the strongest electric fields were found at the tips of the rod, and the induced electric field patterns under σ^- and σ^+ did not overlap. The difference was further revealed by calculating the results of $2(|E_{\sigma^-}|^2 - |E_{\sigma^+}|^2)/(|E_{\sigma^+}|^2 + |E_{\sigma^+}|^2)$, mimicking the g–factor. The diagrams clearly demonstrated the changes in the electric field induced by σ^- and σ^+ shown in Figs. S1(a_3, b_3, c_3).

A0.2 SEM images, Optical measures

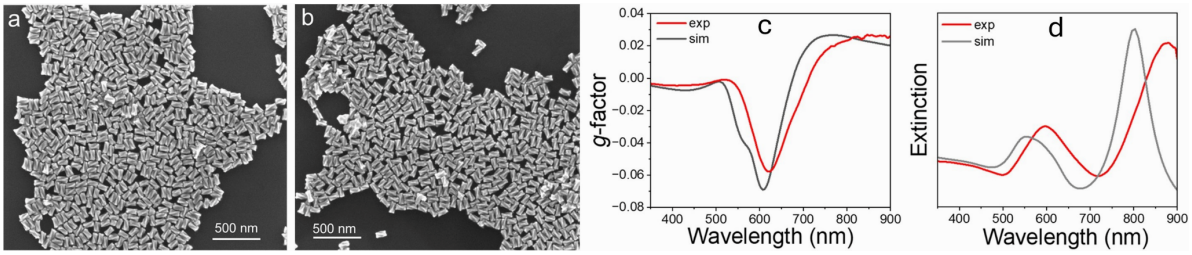

Fig. S2. SEM images and optical simulation and experimental results. (a, b) Low magnification SEM of the left-handed and right-handed twisted gold NRs. (c, d) Optical simulation and experimental results based on the right-handed twisted gold NR obtained via electron tomography result. The gray lines indicate the simulation results, while the red lines indicate the experimental results.

Low-magnification SEM images exhibit dense carpets of left and right handed twisted gold nanorords within a few hundreds of nanometers and distinct "enatiometeric" surface morphologies (Fig. S2 a,b). The g-factor (CD) spectrum show experimental results (Fig. S2 c) and simulation (d) show similar pronounced negative band peaks near 650 nm confirming the strong plasmon - enchanced circular dichroism of the chiral NRs. These characterization verifies the optical activity predicted by the electromagnetic simulations.

A0.3 Experimental Setup

For the sample preparation of the experiment, the thick nanoparticles were deposited onto a glass slide with a micropipette. Subsequently, the nanoparticles were dispersed by a spin coater at a relatively low speed.

Figure S3 is an illustration of the experimental setup. The laser is a mode-locked regenerative Ti: sapphire laser producing approximately 100 femtosecond pulses at a repetition rate of 1 kHz with 804 nm center wavelength. Laser pulses traverse a half-wave plate (HWP) in combination with a quarter-wave plate (QWP) that controls the polarization state of the laser beam. These polarization states include linearly polarized light ($\sigma^0 = 0$) and circularly polarized light ($\sigma^{\pm} = \pm 1$). Under a transmission geometry, the laser beam is focused by a first lens onto the nanoparticles after passing through polarization optics (half-wave plate pate and quarter-wave plate). Polarization optics enables the illumination of nanoparticles with the laser beam of various polarizations, including linear and circular ones. We use a spatial light modulator (SLM), which is an optical device that dynamically modulates the phase, and intensity of the incident beam spatially. The SLM is employed as a reflective optical element to facilitate the reflection of the fundamental beam and the generation of customized beam patterns to create beams that carry orbital angular mo-

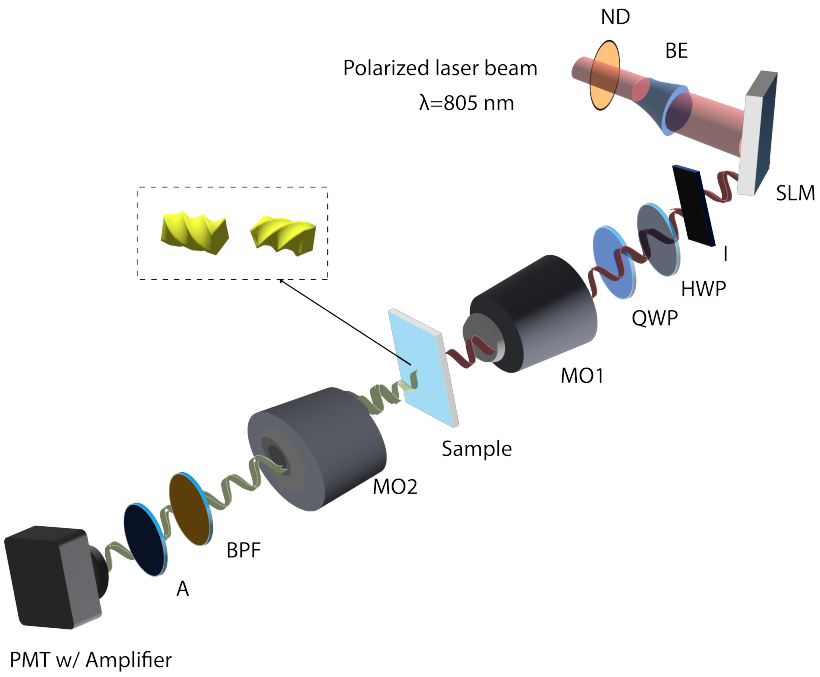

Fig. S3. Experimental setup for TPL measurement and helical dichroism determination. The combination of the HWP and QWP enables the generation of linearly polarized or circularly polarized light. The SLM (Santec-200) enables the production of structured light carrying non-zero orbital angular momentum (OAM). The iris serves as a spatial filter to the first-order that is then focused by a 100× 0.90NA dry objective lens onto the sample on a glass slide and the photoluminescence is collected by a 50× 0.80NA microscope objective.

mentum (OAM). An iris is employed to block the zeroth order and select the preferred order of the OAM beam. No iris is required for testing with the reflection of the fundamental beam. A 100× 0.90 NA dry objective lens is used to focus the beam onto the sample, and the collection is done by a 50× 0.80 NA dry objective lens. The sample is placed on a (x, y, z) translation stage. A (550±25 nm) bandpass filter along with an analyzer rejects fundamental light, allows the nonlinear emissions, and selects the preferred polarization state of the signals. A Thorlabs High-Speed Si Photodetector with a PDA200C photodiode Amplifier enables low noise measurements of small photodiode currents. To minimize sample damage, the laser power used is < 2.5 mW.

Light beams carrying spin and/or orbital angular momentum were controlled by SLM and a combination of polarization optics (Linear Polarizers (LP), HWP, QWP). When a Gaussian beam is incident on the SLM with a phase mask, an optical vortex with a phase singularity of a certain topological charge (ℓ) can be generated.

A0.4 Different emission of Two-photon processes

In a nonlinear media, the dielectric polarization (P) is nonlinearly related to the incident light's electric field (E). The parametric process is generally coherent. Many parametric nonlinear processes depend on phase matching condition and are usually polarization dependent. Because of the nature of the electronic energy levels involved in the photon absorption during the nonlinear process, one can distinguish a parametric process from non-parametric ones. If the excited state is virtual, the process is parametric ($\omega_3 = \omega_1 \pm \omega_2$). Otherwise, it is a nonparametric process ($\omega_3 < \omega_1 + \omega_2$).

Two-Photon Processes		Excitation wavelength (λ_ω)	Emission wavelength ($\lambda_{\omega'}$)	Degree of Nonlinearity
TPA	TPL	800 nm [1] 774 nm [2] 800 nm [3]	620 nm [1] 610 nm [2] ∼650 nm [3]	2.05±0.01 [1] 1.93±0.04 [2] 1.97 [3]
	TPE	760 nm (785 nm) [4]	[555, 728] nm [4]	2.07 (2.10) [4]
SHG		850 nm [5]	425 nm [5]	2.2 [5]

Table 1: **Two-photon absorption and degree of nonlinearity.**

Two-photon absorption (TPA) is a nonlinear optical process dependent on the third-order nonlinear susceptibility ($\chi^{(3)}$). The relationship between the number of photons, equivalently, order of the electronic transitions involved in a TPA process and the order of the corresponding nonlinear susceptibility is misleading. Likewise, the relationship between input power and generated fluorescence power is most of the time quadratic, further increasing the ambiguity. Experimentally, the fluorescence spectrum, the input/output power relationship, and the material's symmetry allow the identification and differentiation of parametric processes from non-parametric nonlinear ones.

A0.5 TPL excited by a Gaussian beam linearly polarized

Two-photon photoluminescence was verified from left-handed and right-handed twisted gold NRs by measuring the dependence of the luminescence intensity ($\lambda_{em} = 550$ nm) as a function of the fundamental power ($\lambda_{ex} = 804$ nm). Signal intensities were collected for light that has linear polarization and circular polarization. In nonlinear optics, the output intensity is related to the input light intensity by a power-law dependence ($I_{out} \propto I_{in}^n$) where the exponent (n) represents the order of the nonlinear process. Consequently, the slope of a log–log plot provides information about the nonlinearity order. A quadratic dependence of the signal intensity was observed as shown in Fig. S4a for linearly polarized Gaussian fundamental beams. The slope values after the conversion into a log-log plot were 1.84 and 1.80 for right and left- handed twisted NRs respectively as shown in Fig. S4b.

The difference between the left and the right handed twisted NRs "slopes" is not accidental as the curves are an average of five different measurements made on the same sample on different NRs. The slope difference may be due to the quality of the particles or to absorption dependent- chirality.

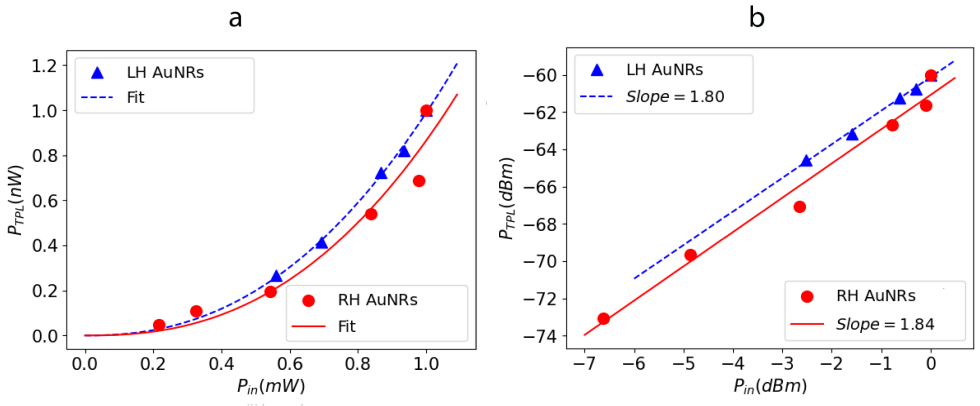

Fig. S4. Quadratic relationship between the TPL power and the Gaussian fundamental power. (a) TPL power as a function of the input power. (b) Log-log plot showing the slope values. The quadratic curves show a slope equal to 1.84 for right and 1.80 for left handed twisted NR indicating a second- order nonlinear TPL response.

A0.6 TPL excited by a Gaussian beam circularly polarized

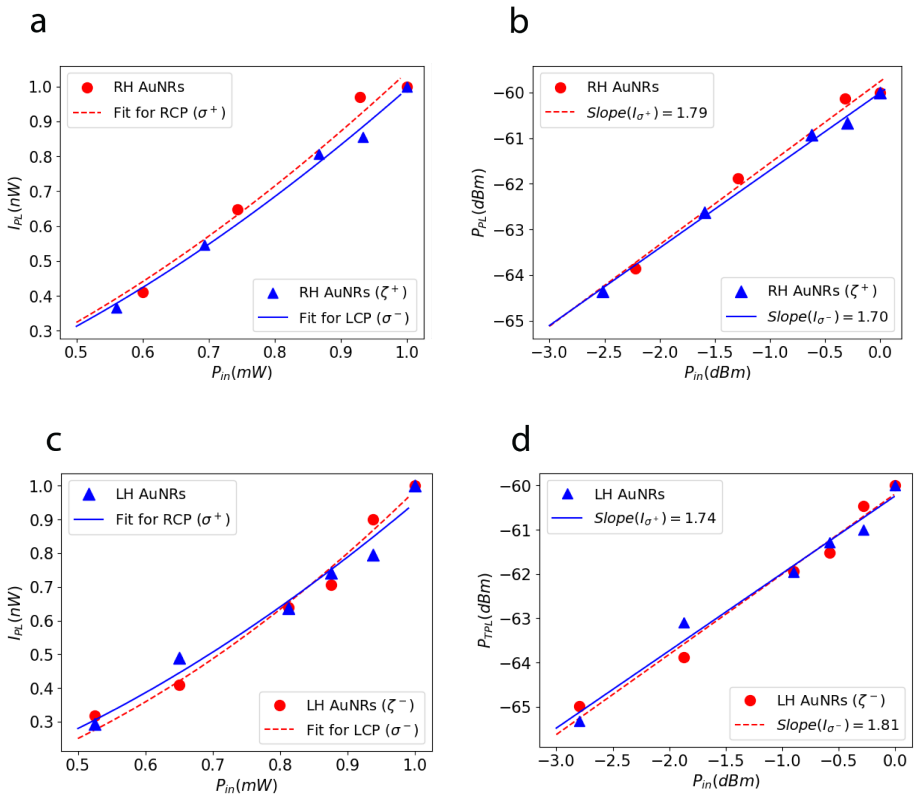

Fig. S5. Quadratic relationship under Gaussian beam circularly polarized. (a,c) Quadratic relationship between TPL power and fundamental circularly polarized Gaussian beam illuminating right-handed twisted gold NR in (a) and the left-handed twisted gold NR in (b). (b,d) Log-log plot showing the slope values in (a) and (b) respectively. In (b), the right-handed twisted gold NRs under RCP-σ^+ (LCP-σ^-) give a slope of 1.79 (1.70). In (d), the left-handed twisted gold NRs under σ^+(-σ^-) excitation gives a slope equal to 1.74 (1.81).

To investigate the difference between the slopes in Fig. S5(b,c), that may reveal the intrinsic dichroism of the twisted gold NRs , we endow the fundamental beam with a spin angular momentum (SAM) by circularly polarizing it. A Gaussian beam circularly polarized possesses a spin momentum $\sigma^{\pm} = \pm 1$. Comparing slopes of curves in Fig. S5, we observe that the slope of the curve for the right-hand (RH) twisted gold NR under RCP (σ^{+}) light is relatively higher as well as that of the left-hand (LH) twisted gold NR under LCP light (σ^{-}). Remarkably, the shining of circularly polarized light onto gold NRs reveals the preferential coupling of gold NRs to light with a certain spin-orbital momentum ($\sigma^{\pm} = \pm 1$). During analysis, the background intensity is subtracted from the measured values to obtain the corrected signal.

A0.7 Asymmetric Laguerre-Gaussian Beam and singularity Shift

The complex amplitude of a conventional LG beam in polar coordinates on the $z = 0$ plane is given by (S5):

$$E_{\ell,p}(r,\varphi,z=0) = \left(\frac{\sqrt{2}r}{w_0}\right)^{|\ell|} \mathcal{L}_p^{\ell}\left(\frac{2r^2}{w_0^2}\right) \exp\left(-\frac{r^2}{w_0^2} + i\ell\varphi\right) \tag{S5}$$

where (r,φ,z) are cylindrical coordinates , w_0 is the Gaussian beam waist, ℓ is the topological charge of the optical vortex and $\mathcal{L}_p^{\ell}$ is the adjoint Laguerre polynomial. If the beam phase is offset by δ from the origin of the x and y coordinate axes (δ can take real or complex values), the complex amplitude takes the following form (S6) [6] for propagation in the free space at an arbitrary distance z

$$\begin{aligned} \Omega_{\ell,p}(s,z) &= \left(\frac{w_0}{w(z)}\right)\left(\frac{\sqrt{2}}{w_0}\right)^{|\ell|} [(x\pm\delta)+i(y\pm\delta)]^{|\ell|}\, \mathcal{L}_p^{\ell}\left(\frac{2s^2}{w^2(z)}\right) \\ E_{\ell,p}(s,\varphi,z) &= \Omega_{\ell,p}(s,z) \exp\left(-\frac{s^2}{w^2(z)} + i\frac{ks^2}{2R(z)} - i(|\ell|+2p+1)\zeta(z)\right) \end{aligned} \tag{S6}$$

Here, $w(z) = w_0\sqrt{1+\left(\frac{z}{z_0}\right)^2}$ with the Rayleigh range $z_0 = \frac{\pi w_0^2}{\lambda}$ at a certain wavelength λ, $s^2 = (x\pm\delta)^2 + (y\pm\delta)^2$ is the new radius, $R(z) = z\left(1+\frac{z_0}{z}\right)^2$ is the radius of curvature, and $\zeta(z) = \arctan\left(\frac{z}{z_0}\right)$ is the Gouy phase shift of a Gaussian beam (the generalization for a Laguerre Gaussian beam, Gouy phase is $(|\ell|+2p+1)\zeta(z)$).
The optical helicity is not noticeable for $\delta_1 \in [-5,5]$ nm and clearly noticeable $\delta_2 \in [-30,30]$ nm as shown in Fig. S6. The difference in the response of right-handed twisted gold NRs and left-handed twisted gold NRs is sensitive to the incident light polarization. Laguerre-Gaussian beams are offset by maintaining a real counterpart while increasing the imaginary or complex component of the other axis.
Considering corrections that can be made in the paraxial regime as well as in the Fourier plane, the longitudinal component of the field is considered as shown in equation (S7) [7, 8]. The asymmetry parameter, δ, displaces the phase singularity causing the electric field amplitude to be asymmetric. For a symmetric LG, $\delta = 0$ but in the case of aLG, $\delta \neq 0$.

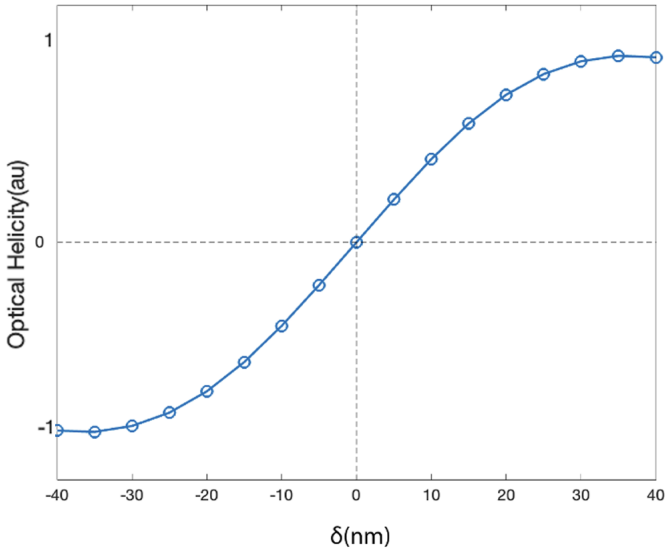

Fig. S6. Numerical simulation of helical dichroism (HD) in nanoparticles.

The displacement is done by offsetting δ on the (x, y) plane considering that it is perpendicular to the polarization direction. Helical dichroism (HD) -type I is defined as:

$$HD_{\ell,p}(s, \varphi, z) = \int_{-w_0}^{+w_0} \mathcal{D}\left(\Upsilon^{+} - \Upsilon^{-}\right) dxdy \tag{S7}$$

where the optical helicity $\Upsilon^{\pm} = Re[\nabla_i E_j^{\pm} E_i^{\pm *}]$ quantifies the handedness of helical light and $\mathcal{D}$ represents a collection of physical quantities or material-dependent prefactors [9]. The $\pm = sign(\ell)$ represents the topological charge (ℓ) polarity of a vortex beam without radial mode $p = 0$.

HD -Type I in equation (S7) is directly proportional to the difference in the inter-band transition rates under excitations by left-handed and right-handed helical beams with asymmetry parameter (δ). It shows that the differential absorption of left-handed and right-handed helical light by achiral and chiral medium can be precisely adjusted by offsetting the singularity (δ) from the cetner of an OAM beam. The simulation results shown in Fig. S6 are obtained by integrating HD -Type I over the entire beam cross section. It shows the evolution of the optical helicity in gold NRs with the offset in an aLG beam.

As seen in the Fig.S6 , helical dichroism is zero for a symmetric LG beam ($\delta = 0$) but is non-zero for aLG beams that exhibit the differential absorption by gold NRs. It is therefore dependent on the beam profile and does not manifest itself in symmetric LG beams.

A0.8 Intensity and electric field profiles of asymmetric Laguerre-Gaussian beam

The interference between aLG and Gaussian beams shows the rotation direction of the electric field, thereby the torque. These offsets induce the redistribution of the ring energy in aLG beams, as shown in Fig. S7.

Unlike conventional LG beams, the transverse intensity patterns clearly show that the electric field is the key. From Fig. S7, when the offset is opposite to the combination ℓ and

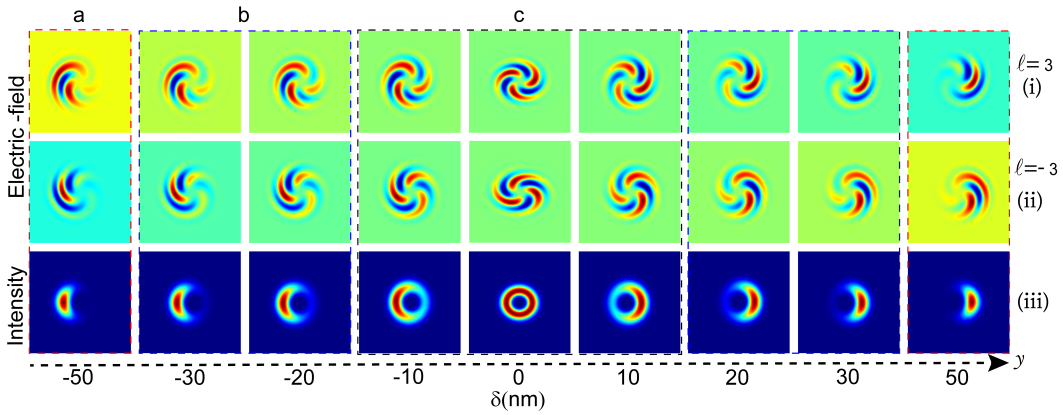

Fig. S7. aLG$_{\pm 3,0}$ beam interfering with a Gaussian beam at the sample Plane. Numerically computed electric field and intensity profile of the fundamental beam aLG$_{\pm 3}$ interfering with a Gaussian beam at the plane of the sample for a singularity offset of (a) $\delta = \pm 50$ nm, (b) $\delta = \pm 30$ nm and $\delta = \pm 20$ nm, and (c) $\delta = \pm 10$ nm. The helicity is less sensitive to the chirality as the asymmetry degree or the singularity offset is low. Above 50 nm, the beam is losing its vortex property.

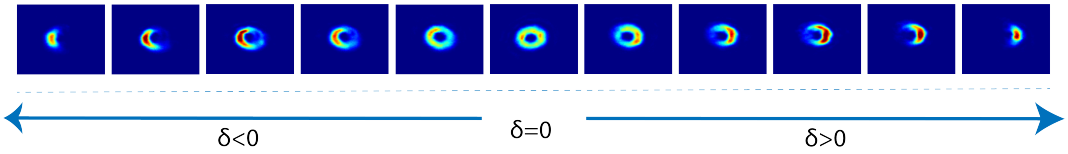

Fig. S8. aLG$_{\pm 3,0}$ experimental images. Intensity profiles of the fundamental beam aLG$_{\pm 3}$ with increasing(to the right) and decreasing(to the left) offset of the singularity.

σ, the electric field changes its polarity (direction). Therefore, the beam interaction with electrons will change depending on the chirality and the coupling with electron OAM. The change in field distribution is confirmed by the experimental data in Fig. S8 as the phase singularity increases or decreases.

A0.9 Choice of the Singularity offset and the topological charge

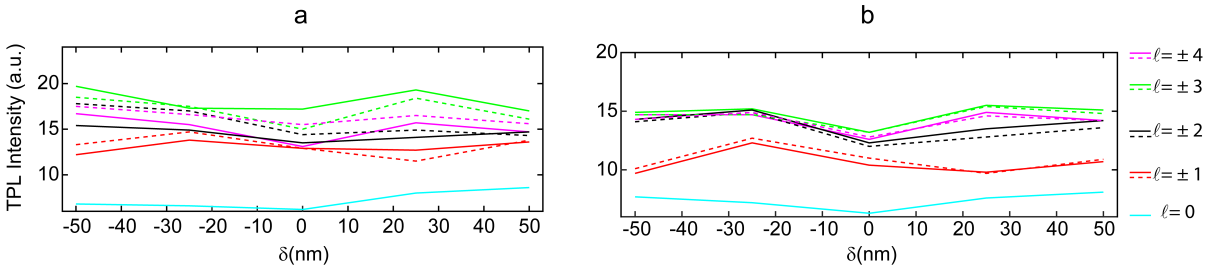

Fig. S9. TPL intensity versus topological charge and the singularity offset. TPL intensity as a function of the singularity offset for different topological charges illuminating (a) left-handed and (b) right-handed twisted gold NRs. The maximum of the intensity is found for $|\ell| = 3$ under a singularity offset different for left-handed ($|\delta| = 30$ nm) and right-handed ($|\delta| = 20$ nm) gold NR. The gap between the maximum singularities that correspond to the maximum intensity may be due to quality difference between the left-handed and right-handed twisted particles.

The phase singularity was displaced systematically by displaying onto the SLM phase masks. As the beam is focused onto the sample, the step size is modulated and the two photon-induced photoluminescence is studied. The singularity in the input OAM beam is varied by displacing the imaginary axis (corresponding to the y-axis) and maintaining a constant position along the real axis. The first part of the study involves the investigation of the transmission properties of two-photon induced photoluminescence in gold NRs by systematically varying the displacement of the optical field's singularity along the imaginary axis while maintaining a constant position along the real axis.
As seen in Fig. S9, the input topological charge (ℓ) is varied between $\ell = [-4, 4]$. The initial profiles showed that the highest transmission of two-photon luminescence (TPL) was observed for topological charge values of $|\ell| = 3$. Expanding on this preliminary finding, we conducted a more detailed investigation of the transmission intensity.

A0.10 Helical dichroism under circularly polarized aLG beams

Circular polarization in conjunction with OAM ($\ell = \pm 3$) is used to study the helical dichroism of twisted gold NRs. HD (circularly polarized) is the difference in absorption (emission) of a circularly polarized light by a chiral solid [10].

$$HD_{CP} = 2\frac{I(\ell, \sigma^{\pm}) - I(-\ell, \sigma^{\mp})}{I(\ell, \sigma^{\pm}) + I(-\ell, \sigma^{\mp})} \tag{S8}$$

Equation (S8) defines the helical dichroism that arises from the differential absorption of helical light endowed with an opposed topological charge ($\ell = \pm 3$) under circular polarization ($\sigma = \pm 1$) . The difference in the TPL intensity for left-handed and right-handed gold NRs in Fig. S9 is captured further by Fig. S10.

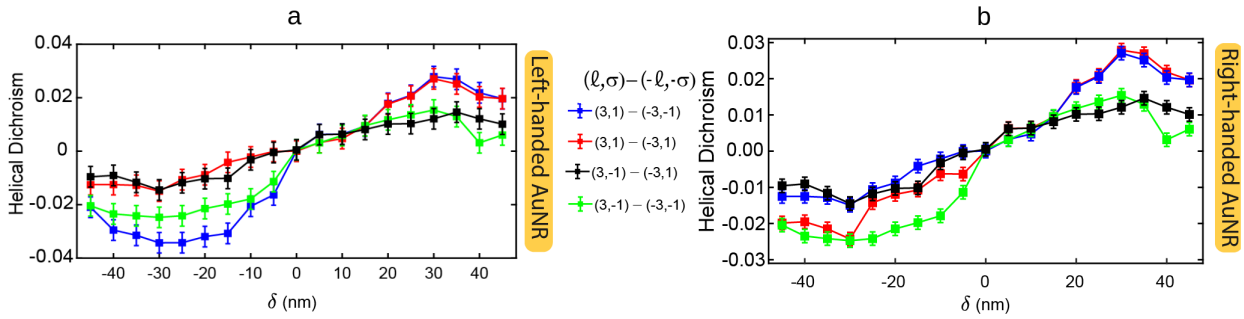

Fig. S10. Chirality handedness and Helical dichroism method. Helical dichroism (CP) as a function of the singularity offset (δ). in (a)left-handed and (b) right-handed (bottom) twisted gold NR probed by various combinations of asymmetric twisted circularly polarized light.

A0.11 Polarization of TPL generated by twisted gold nanorods

The polarization-dependent nonlinear response was measured by rotating the incident polarization with a half-wave plate, while detecting the emission through a fixed analyzer orientation.
Fig. S11 represents the remaining possible combinations shown in the main text. It shows clearly that when the product of two phase offsets is negative ($\delta_1\delta_2 < 0$), the magnitude of

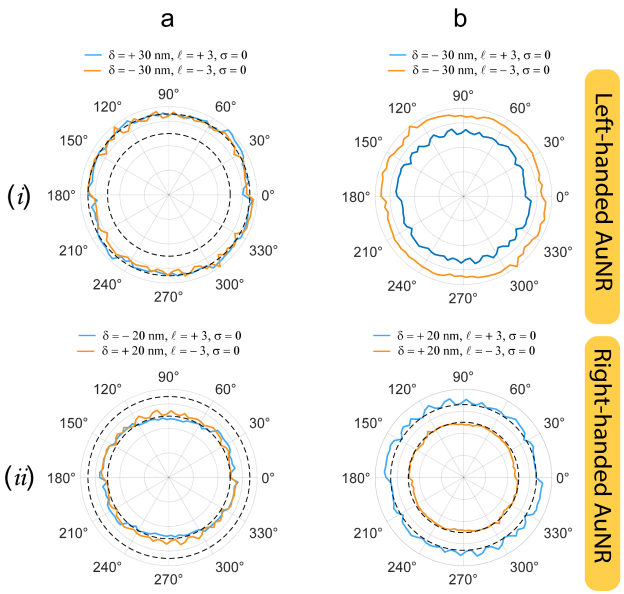

Fig. S11. Vortex offset combination and TPL polarization under linearly polarized aLG beams. (a,b) Polarization and magnitude of TPL intensity under aLG beams with opposite polarity in δ (a) and the same polarity in δ (b). Each point in the graph is an average of five measurements taken under the same condition on the same sample. For clarity, the standard error is not added.

the TPL is the same – the absorption is at the same level for beam with $|\ell| = 3$. Discontiguous TPL curves appear only when the product of phase offsets is positive ($\delta_1\delta_2 > 0$).

A0.12 Multiphoton Imaging and Emission Spectrum : Fluorescence images and Emission Spectrum

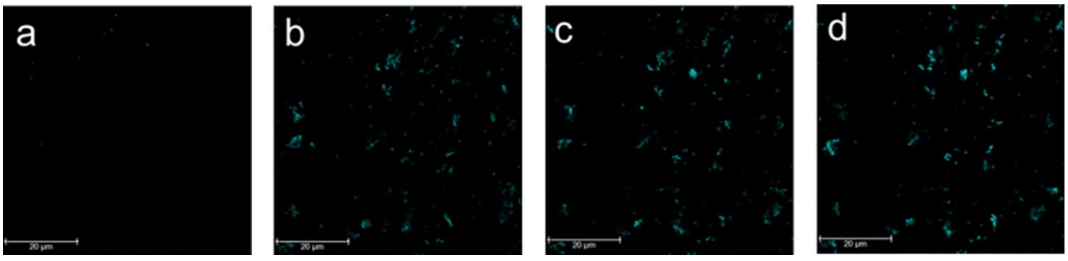

Fig. S12. Microscopic images of the right-handed twisted gold NRs under irradiation of 900 nm. (a) second-harmonic generation 450 nm. (b–d) TPL wavelengths detected at 475 nm (b), 500 nm (c), and 525 nm (d).

Further analysis was performed with a Leica confocal microscope SP8 which has a femtosecond laser (Chameleon, $\lambda = 900\ nm$) installed within the system, to study nonlinear optical emissions. By changing emission filters, different intensity distribution images were obtained as shown in Fig. S12. Nonlinear emissions include second harmonic generation (exactly half of the initial wavelength λ_{in}) and two-photon photoluminescene ($> \frac{1}{2}\lambda_{in}$) from the right-handed twisted gold NRs. Also, the acquired emission spectrum shows two (2) major peaks at approximately 540 nm and 610 nm and correspond to the plasmonic

resonance features observed in the absorbance spectra of left- and right-handed nanoparticles, as well as gold NRs with varying aspect ratios [11, 12].

References

[1] Jeremy W Jarrett, Tian Zhao, Jeffrey S Johnson, Xiaoying Liu, Paul F Nealey, Richard A Vaia, and Kenneth L Knappenberger Jr. Plasmon-mediated two-photon photoluminescence-detected circular dichroism in gold nanosphere assemblies. *The journal of physical chemistry letters*, 7(5):765–770, 2016.

[2] Artur Movsesyan, Gwénaëlle Lamri, Sergei Kostcheev, Anke Horneber, Annika Bräuer, Alfred J Meixner, Monika Fleischer, Dai Zhang, Anne-Laure Baudrion, and Pierre-Michel Adam. Enhanced two-photon photoluminescence assisted by multi-resonant characteristics of a gold nanocylinder. *Nanophotonics*, 9(12):4009–4019, 2020.

[3] Xiao-Fang Jiang, Yanlin Pan, Cuifeng Jiang, Tingting Zhao, Peiyan Yuan, T Venkatesan, and Qing-Hua Xu. Excitation nature of two-photon photoluminescence of gold nanorods and coupled gold nanoparticles studied by two-pulse emission modulation spectroscopy. *The journal of physical chemistry letters*, 4(10):1634–1638, 2013.

[4] Xuxing Lu, Deep Punj, and Michel Orrit. Two-photon-excited single-molecule fluorescence enhanced by gold nanorod dimers. *Nano Letters*, 22(10):4215–4222, 2022.

[5] Guang-Can Li, Dangyuan Lei, Meng Qiu, Wei Jin, Sheng Lan, and Anatoly V Zayats. Light-induced symmetry breaking for enhancing second-harmonic generation from an ultrathin plasmonic nanocavity. *Nature communications*, 12(1):4326, 2021.

[6] A. A. Kovalev, V. V. Kotlyar, and A. P. Porfirev. Asymmetric laguerre-gaussian beams. *Physical Review A*, 93(6):063858, 2016.

[7] Alexander Cerjan and Charles Cerjan. Orbital angular momentum of laguerre–gaussian beams beyond the paraxial approximation. *JOSA A*, 28(11):2253–2260, 2011.

[8] Kayn A Forbes, Dale Green, and Garth A Jones. Relevance of longitudinal fields of paraxial optical vortices. *Journal of Optics*, 23(7):075401, 2021.

[9] Jean-Luc Bégin, Ashish Jain, Andrew Parks, Felix Hufnagel, Paul Corkum, Ebrahim Karimi, Thomas Brabec, and Ravi Bhardwaj. Nonlinear helical dichroism in chiral and achiral molecules. *Nature Photonics*, 17(1):82–88, 2023.

[10] Ashish Jain, Jean-Luc Bégin, Paul Corkum, Ebrahim Karimi, Thomas Brabec, and Ravi Bhardwaj. Intrinsic dichroism in amorphous and crystalline solids with helical light. *Nature Communications*, 15(1):1350, 2024.

[11] Ji-Young Kim, Jihyeon Yeom, Gongpu Zhao, Heather Calcaterra, Jiyoun Munn, Peijun Zhang, and Nicholas Kotov. Assembly of gold nanoparticles into chiral superstructures driven by circularly polarized light. *Journal of the American Chemical Society*, 141(30):11739–11744, 2019.

[12] Catherine J Murphy, Lucas B Thompson, Davin J Chernak, Jie An Yang, Sean T Sivapalan, Stefano P Boulos, Jingyu Huang, Alaaldin M Alkilany, and Patrick N Sisco. Gold nanorod crystal growth: From seed-mediated synthesis to nanoscale sculpting. *Current Opinion in Colloid & Interface Science*, 16(2):128–134, 2011.